



Synthesis of Novel $ZrO_2/g-C_3N_4/CuFe_2O_4$ Nanocomposite and Its Efficient Photocatalytic Degradation of Amoxicillin, Chlorpyrifos and Methylene Blue

PANDURANGAN VIJAYALAKSHMI¹, POOVAN SHANMUGAVELAN^{1,*}, PAULPANDIAN MUTHU MAREESWARAN² and KIRUTHIGA KANDASAMY²

¹Department of Chemistry, School of Science, Tamil Nadu Open University, Chennai-600015, India

²Department of Chemistry, College of Engineering, Anna University, Chennai-600025, India

*Corresponding author: E-mail: drpshanmugavelan@tnou.ac.in

Received: 8 December 2023;

Accepted: 6 February 2024;

Published online: 28 February 2024;

AJC-21564

A novel $ZrO_2/g-C_3N_4/CuFe_2O_4$ nanocomposite was synthesized by wet impregnation method and its photocatalytic degradation efficacy is studied on the organic pollutants *viz.* antibiotic drug (amoxicillin), pesticide (chlorpyrifos) and dye (methylene blue) under both dark and visible light conditions in liquid medium. The synthesized nanocomposite and its photocatalytic degradation studies were well characterized using XRD, TEM, EDS, XPS, UV-Vis DRS, PL, BET and EIS analytical techniques. Among three organic pollutants, the photocatalytic degradation of methylene blue pollutant is higher (99.5%, $k = 0.0533 \text{ min}^{-1}$) than that of chlorpyrifos (97.3% $k = 0.0367 \text{ min}^{-1}$) and amoxicillin (64.6%, $k = 0.0109 \text{ min}^{-1}$) under visible light exposure for 90 min using $ZrO_2/g-C_3N_4/CuFe_2O_4$ nanocomposite as a photocatalyst. The nanocomposite showed excellent degradation efficiency under the irradiation of visible light while the degradation under dark condition is highly limited. As a control experiment the individual $g-C_3N_4$, ZrO_2 and $CuFe_2O_4$ components of the nanocomposite under the same conditions possess limited degradation efficiency than that of $ZrO_2/g-C_3N_4/CuFe_2O_4$ nanocomposite. A possible photo-degradation mechanism is also proposed. Efficient treatment of wastewater could be possible with this novel nanocomposite $ZrO_2/g-C_3N_4/CuFe_2O_4$ due to its high stability and reusability.

Keywords: Degradation, Nanocomposite, Organic pollutants, Photocatalyst, Wet impregnation method.

INTRODUCTION

Water quality is an important parameter which is mostly influenced by the industrial pollution [1-5]. Textile dyes, antibiotics, insecticides and fertilizers are the important categories of pollutants of water due to industrialization [6-12]. One of the important methods to address this problem is photocatalytic degradation. Graphitic carbon nitride ($g-C_3N_4$), a conjugated polymer of metal-free attractive, which is inexpensive, benign and thermally as well as chemically stable with a sufficient band-gap (2.7 eV) has the subject of extensive research in recent years [13]. The photocatalytic activity of $g-C_3N_4$ has enhanced when they are converted into composites like $g-C_3N_4/Mn-ZnO$, $g-C_3N_4/TiO_2/\alpha-Fe_2O_3$, etc. [14].

ZrO_2 stands out as a promising photocatalyst due to its affordability, non-toxic nature, high-temperature stability, strength and reusability [15,16]. However, ZrO_2 systems suffer from significant drawbacks, including their limited sensitivity

to visible light due to a high bandgap ranging from 5.00 to 5.18 eV, as well as slow generation, rapid recombination of electron-hole pairs (e^-/h^+) [17,18]. Electro doping these less efficient metal oxide systems with metal and non-metal dopants in $g-C_3N_4$ and $CuFe_2O_4$ is an effective way to decrease these defects [19,20].

Due to its low cost, high photochemical stability and sensitivity to visible light, the magnetic oxide semiconductor $CuFe_2O_4$ is considered one of the most effective co-catalysts. Furthermore, due to the high rate of electron-hole pair recombination, $CuFe_2O_4$ alone only displayed a modest amount of photocatalytic activity when exposed to visible light. Therefore, creating fresh visible-light-driven photocatalysts that are effective and reusable poses a significant challenge for energy conservation and environmental restoration [21,22]. Hence, the combination of these materials can be envisaged to provide higher efficiency towards photocatalytic degradation.

Hence, we herein report the synthesis of novel $ZrO_2/g-C_3N_4/CuFe_2O_4$ nanocomposite by wet impregnation method

and studied the photocatalytic degradation efficacy on organic pollutants such as a drug (amoxicillin), a dye (methylene blue) and a pesticide (chlorpyrifos) under both dark and light conditions.

EXPERIMENTAL

All the chemicals and reactants used in this research were analytically pure without any further purification (A.R. grade). Urea ($\text{CH}_4\text{N}_2\text{O}$, Merck, 99.5% purity), citric acid monohydrate ($\text{C}_6\text{H}_{10}\text{O}_8$, Merck, 99% purity), chemical grade iron(III) nitrate nonahydrate [$\text{Fe}(\text{NO}_3)_3 \cdot 9\text{H}_2\text{O}$] and copper(II) nitrate hexahydrate [$\text{Cu}(\text{NO}_3)_2 \cdot 6\text{H}_2\text{O}$], sodium hydroxide (Merck, 97% purity) and hydrochloric acid (ADWIC 33%), ethylenediamine, zirconyl nitrite ($\text{ZrO}(\text{NO}_3)_2$) were obtained from Sigma-Aldrich, USA. Isopropyl alcohol (Sigma-Aldrich), 1,4-benzoquinone (BQ, Alfa Aesar, Massachusetts) and ethylenediaminetetraacetic acid (EDTA) were obtained from Sigma-Aldrich and used for the scavenger analysis. The antibiotic drug *viz.* amoxicillin (AMX, 500 mg), methylene blue (MB) dye and pesticide chlorpyrifos (CPF, 500 mL) were used as pollutants. Millipore distilled water and deionized water was used throughout the experiment.

Synthesis of $\text{ZrO}_2/g\text{-C}_3\text{N}_4/\text{CuFe}_2\text{O}_4$ nanocomposite: The synthesis of $\text{ZrO}_2/g\text{-C}_3\text{N}_4/\text{CuFe}_2\text{O}_4$ nanocomposite was achieved by wet impregnation method [18] using CuFe_2O_4 , $g\text{-C}_3\text{N}_4$ and ZrO_2 nanocomponents which were synthesized as based on the earlier reports [10,23-26]. The stoichiometric amount (0.1 mol each) of $g\text{-C}_3\text{N}_4$, ZrO_2 and CuFe_2O_4 were added into 30 mL of ethanol. Then this mixture was continuously stirred at 70 °C for 1 h until evaporation of the solvent. The resulting nanocomposite was then collected, dried overnight and kept for further studies.

Characterization: All the synthesized nanoparticles were characterized using X-ray diffractometer (Bruker Kappa APEX II) to study the crystalline phase structure and phase compositions of the samples with $\text{CuK}\alpha$ emission over the 2θ range of 10-80°. The electrochemical impedance spectroscopy (EIS, Princeton, NJ, USA) was used to analyze electrical properties and processes occurring at the interface between an electrode and an electrolyte solution.

The surface morphology, elemental mapping distribution, internal morphology (particle size, shape and distribution), surface chemical bonding and optical properties of the nanocomposite were examined by transmission electron microscopy (TEM, Termo Scientific - Talos F200S), X-ray photoelectron spectroscopy (XPS, Termo Scientific - ESCALAB 250 xi) and UV-vis diffuse reflectance spectra (DRS, Shimadzu/UV 2600 UV-vis spectrophotometer from 400 to 800 nm), respectively. The surface area and pore size distributions were calculated using the Brunauer-Emmett-Teller (BET, Autosorb IQ, USA) method. Photoluminescence (PL, Edinburgh FL/FS900 spectrophotometer with an excitation wavelength of 320 nm) spectra was recorded to find out the interaction among the elements of the nanocomposite.

Photocatalytic degradation of organic pollutants: The photocatalytic degradation of the organic pollutants such as amoxicillin/methylene blue/chlorpyrifos were carried out in a photocatalytic reactor (Heber photoreactor, Annular type, HVAR-MP 400) UV-visible light irradiation is accomplished with a

300 W Xenon lamp and a 420 nm cutting filter, which completely shields the radiation below 420 nm [14].

At the outset, 50 mg of synthesized $\text{ZrO}_2/g\text{-C}_3\text{N}_4/\text{CuFe}_2\text{O}_4$ nanocomposite was added to 100 mL of an aqueous solution of amoxicillin/methylene blue/chlorpyrifos (20 mg/L). Then, the solution was stirred in the dark condition for 0.5 h to attain the adsorption-desorption state of equilibrium. For photocatalytic degradation studies, this solution was kept in a photocatalytic reactor with continuous aerated by pump to make sure that the suspension of catalyst were uniform over the period of reaction. At regular intervals (10 min), adequate amount of sample solution (5 mL) was taken over and centrifuged for 10 min to separate the nanocatalysts for further use. After that the supernatant solution was analyzed with the help of UV-visible double beam spectrophotometer at the wavelength of absorbance maximum (MB $\lambda_{\text{max}} = 664$ nm, AMX $\lambda_{\text{max}} = 341$ nm and CPF $\lambda_{\text{max}} = 291$ nm) to obtain the concentration of pollutants in the solution [6,14].

The percentage of degradation of pollutants has been calculated using the following equation:

$$\text{Degradation (\%)} = \frac{C_0 - C_t}{C_0} \times 100 \quad (1)$$

where C_0 (initial concentration) and C_t (concentration decreases with respect to time, t) represent the levels of organic pollutants both before and after photoirradiation, respectively.

RESULTS AND DISCUSSION

Phase structure analysis: The powder X-ray diffraction (PXRD) studies were conducted to look into the crystalline phase structure of ZrO_2 , $g\text{-C}_3\text{N}_4$, CuFe_2O_4 and nanocomposite $\text{ZrO}_2/g\text{-C}_3\text{N}_4/\text{CuFe}_2\text{O}_4$. Fig. 1a shows that the $g\text{-C}_3\text{N}_4$ develops when

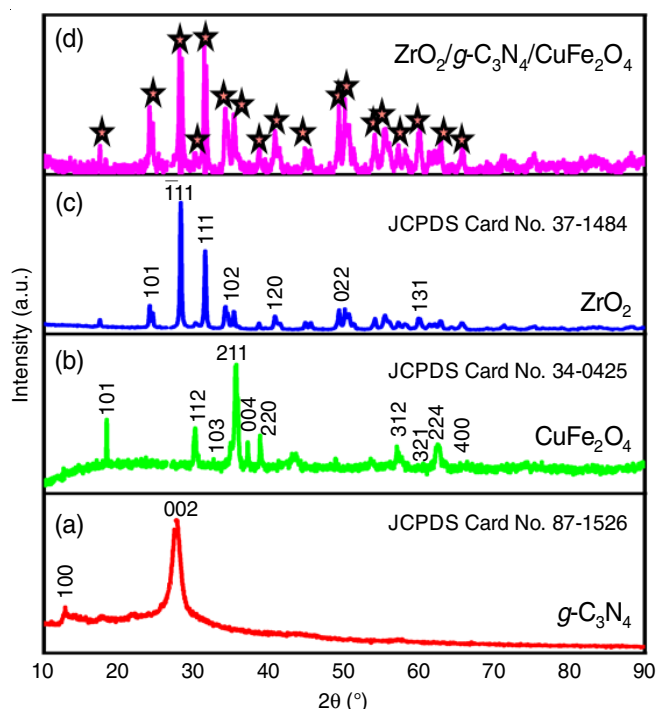


Fig. 1. PXRD pattern of (a) $g\text{-C}_3\text{N}_4$, (b) ZrO_2 , (c) CuFe_2O_4 , (d) $\text{ZrO}_2/g\text{-C}_3\text{N}_4/\text{CuFe}_2\text{O}_4$

urea and citric acid undergoes annealing at 550°C , as seen by the peaks that occur at 12.8° and 27.5° , which corresponding to the diffraction planes (100) and (002) for periodically stacking graphitic material (JCPDS card No. 87-1526) [23,24].

As indicated in Fig. 1b, the diffraction peaks at 2θ values of 28.2° , 31.5° , 38.5° , 50.1° and 59.8° corresponding to the plans to (101), ($\bar{1}11$), (111), (102), (120), (022) and (131) exhibited the rutile phase of ZrO_2 according to the JCPDS card No. 37-1484 [25,26]. Fig. 1c shows the XRD patterns of CuFe_2O_4 with cubic spinel phase (JCPDS 34-0425) show an amorphous structure and distinctive crystal planes (101), (112), (103), (211), (004), (220), (312), (321), (224) and (400). The increased degree of crystallinity that is present in the CuFe_2O_4 is confirmed by sharp peaks presented in the XRD pattern [27,28]. The XRD pattern of $\text{ZrO}_2/g\text{-C}_3\text{N}_4/\text{CuFe}_2\text{O}_4$ nanocomposite (Fig. 1d) confirmed the observation of all of the peaks for each individual nanoparticles (ZrO_2 , $g\text{-C}_3\text{N}_4$ and CuFe_2O_4) and the $\text{ZrO}_2/g\text{-C}_3\text{N}_4/\text{CuFe}_2\text{O}_4$ nanocomposite crystalline size is 24 nm were calculated by using Debye-Scherrer's formula [11].

Morphological structure analysis: The morphologies of synthesized $\text{ZrO}_2/g\text{-C}_3\text{N}_4/\text{CuFe}_2\text{O}_4$ nanocomposite (Fig. 2a-d) were examined using transmission electron microscope (TEM) technique to investigate the crystal structure of $\text{ZrO}_2/g\text{-C}_3\text{N}_4/\text{CuFe}_2\text{O}_4$ nanocomposite. The $g\text{-C}_3\text{N}_4$ sheet was fused with ZrO_2

and CuFe_2O_4 nanoparticles. Due to the sufficient interaction with $g\text{-C}_3\text{N}_4$ sheet, the $\text{ZrO}_2/g\text{-C}_3\text{N}_4/\text{CuFe}_2\text{O}_4$ nanocomposite had the least amount of agglomeration when compared to the individual nanoparticles [29-31]. The nanocomposite of $\text{ZrO}_2/g\text{-C}_3\text{N}_4/\text{CuFe}_2\text{O}_4$ has a larger surface area and active site, which makes it advantageous for charge separation and allows it to degrade AMX/CPF/MB under visible light efficiently [32,33].

The surface area of the nanocomposite and the properties related to porosity dictated that there was less aggregation of spheroidal ZrO_2 and rod-like CuFe_2O_4 nanoparticles on the $g\text{-C}_3\text{N}_4$ nanosheets, respectively [29,31]. Thus, the photodegradation efficiency is enhanced by a wide surface area, low agglomeration, and strong particle-to-particle contact, which reduce the likelihood of photoexcited charge carriers recombining and increases charge transfer [32]. The internal morphology of ZrO_2 and CuFe_2O_4 were distributed over the surface of $g\text{-C}_3\text{N}_4$, which has thin lamellar structure [33-37]. Fig. 2c shows the SAED pattern of $\text{ZrO}_2/g\text{-C}_3\text{N}_4/\text{CuFe}_2\text{O}_4$ nanocomposite was prepared by wet impregnation method. The particle size of $\text{ZrO}_2/g\text{-C}_3\text{N}_4/\text{CuFe}_2\text{O}_4$ nanocomposite was calculated as 27 nm approximately. The SAED pattern of $\text{ZrO}_2/g\text{-C}_3\text{N}_4/\text{CuFe}_2\text{O}_4$ nanocomposite reveals distinct circular diffraction rings, which suggests a high degree of crystallinity and crystalline nature of the nanocomposite.

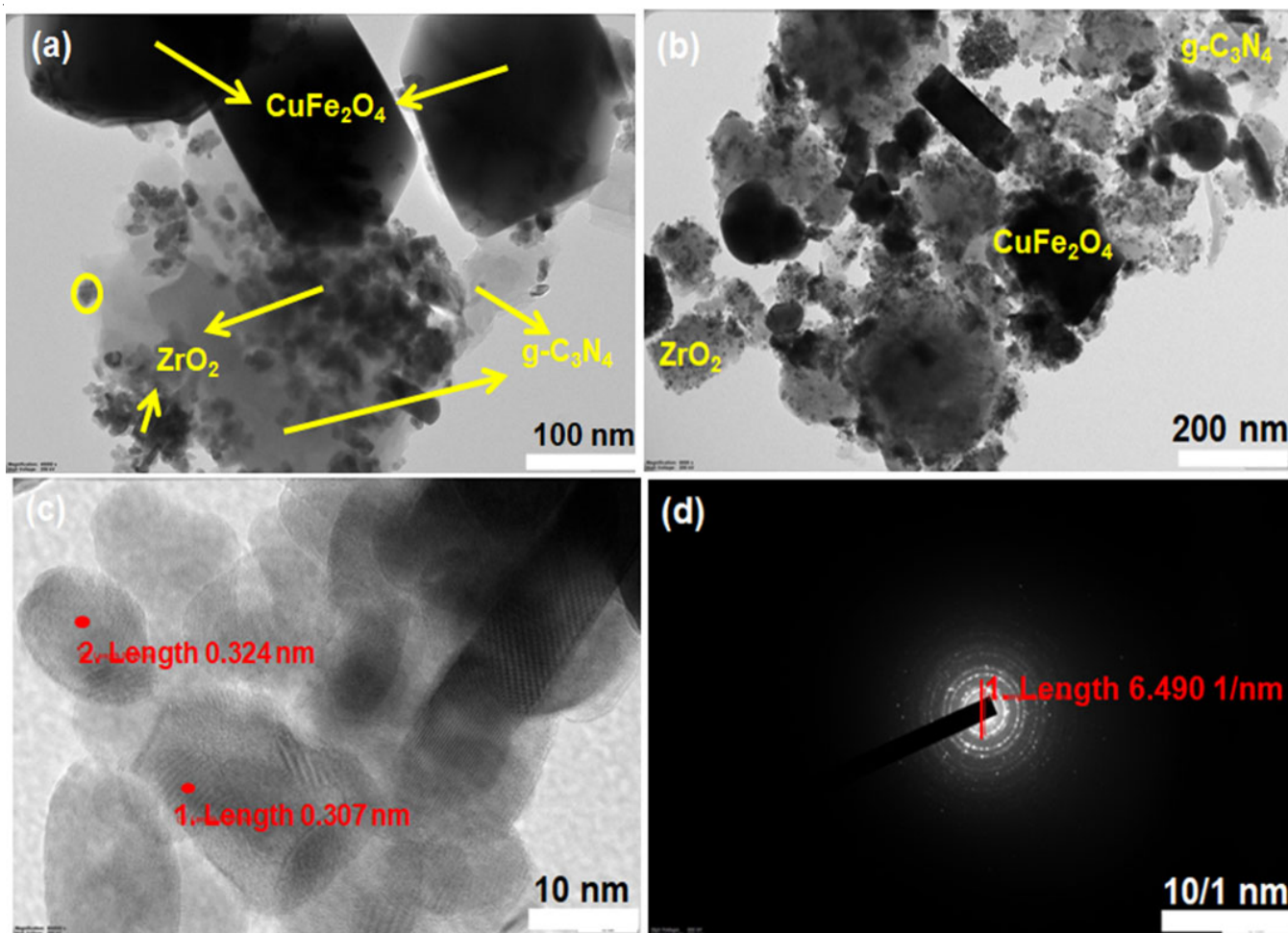


Fig. 2. (a-c) TEM and (d) SAED images of synthesized nanocomposite of $\text{ZrO}_2/g\text{-C}_3\text{N}_4/\text{CuFe}_2\text{O}_4$, ZrO_2 , CuFe_2O_4 and $g\text{-C}_3\text{N}_4$

Surface and elemental composition analysis

X-ray photoelectron spectroscopic (XPS) studies: The X-ray photoelectron spectroscopy (XPS) studies was analyzed to clarify the surface electronic states of tripartite photocatalytic nanocomposite *i.e.* $\text{ZrO}_2/g\text{-C}_3\text{N}_4/\text{CuFe}_2\text{O}_4$. The nanocomposite was composed of six elements *viz.* carbon (C), nitrogen (N), oxygen (O), zirconium (Zr), iron (Fe) and copper (Cu). The XPS survey spectrum of $\text{ZrO}_2/g\text{-C}_3\text{N}_4/\text{CuFe}_2\text{O}_4$ displays the extremely high-resolution XPS spectra of C1s, N1s, O1s, Zr 3d, Fe 2p, Zr 3d and Cu 2p elements (Fig. 3a).

The high resolution C1s spectrum (Fig. 3b) shows two peaks at 288.2 and 284.8 eV. The initial peak has been attributed to sp^2 carbon in the $g\text{-C}_3\text{N}_4$ and benzoic rings as well as C-C bonds while the second peak was assigned to sp^2 hybridized carbon in C-N-C and the N-containing automatic ring (N=C=N) [14].

In the binding energy portion of the N1s spectrum (Fig. 3c) might be deconvoluted into two peaks at 399.8 and 398.4 eV. The first peak is the sp^2 hybridized aromatic (C-N=C) nitrogen bonded to carbon atoms, while the second peak is the 3° nitrogen (N-C3) [10,34]. In (Fig. 3d), the O1s spectrum was divided into two peaks at 531.3 and 533.8 eV wherein the first one is linked to the Zr-O bond, the lattice oxide oxygen species of metal oxides (Fe-O and Cu-O) and the adsorption of hydroxyl groups onto the surface [20] and the second one could be triggered in the water molecule also adsorbed onto the non stoichiometric surface O_2 bond associated with Zr, Cu and Fe. The Zr 3d spectrum (Fig. 3e) shows two typical signals (Zr $3d_{3/2}$ and Zr $3d_{5/2}$) at 183.3 eV and 181.1 eV, which are distinct types of Zr^{2+} [21,36]. For the Fe 2p spectra (Fig. 3f), five peaks have identified at 710.2, 712.0, 718.3, 723.4 and 725.0 eV correspond-

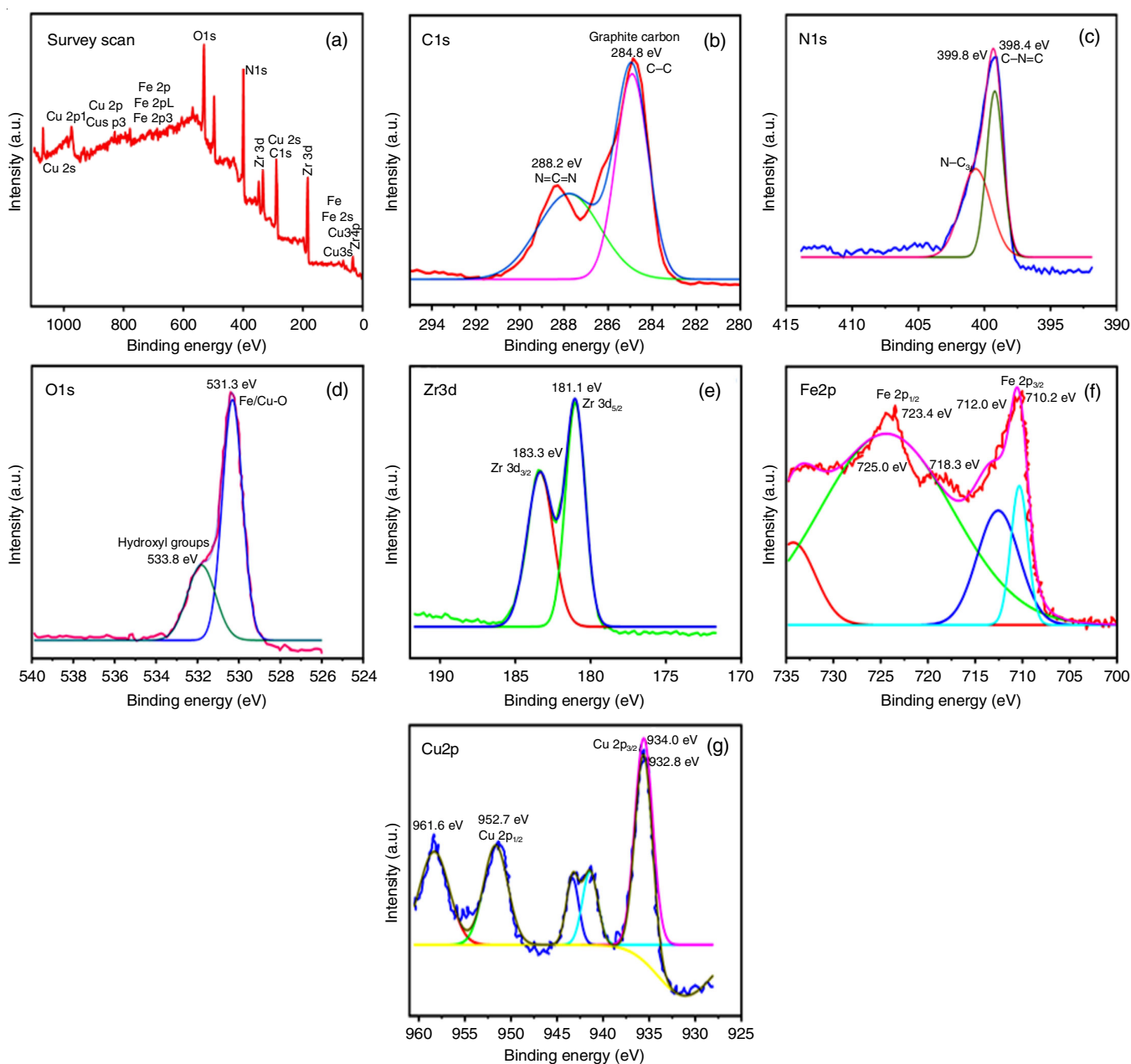


Fig. 3. (a) Survey scan, high-resolution XPS spectra (b) C, (c) N, (d) O, (e) Zr, (f) Fe and (g) Cu for obtained $\text{ZrO}_2/g\text{-C}_3\text{N}_4/\text{CuFe}_2\text{O}_4$ nanocomposite

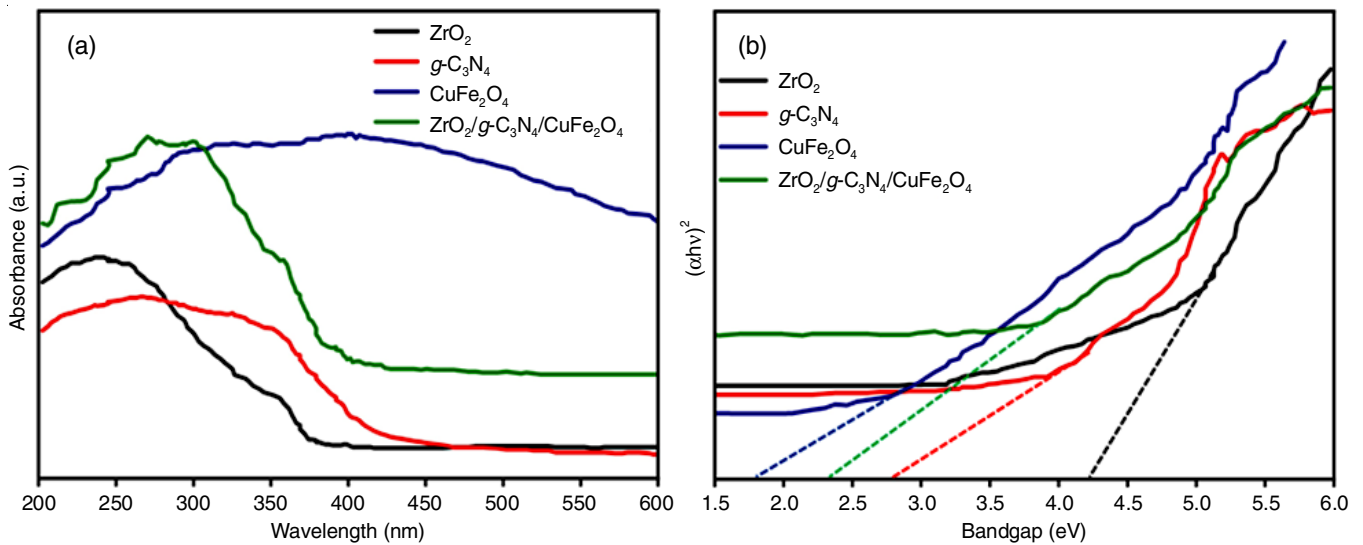


Fig. 4. (a) UV-Vis DRS and (b) the consistent bandgap values *via* Tauc plot of the synthesized nanoparticles

ondingly. The peak near 710.2 eV might be the reason to the binding energies of 2p_{3/2} for Fe³⁺, the peak at 712.0 and 723.4 eV were allotted with the 2p_{3/2} and 2p_{1/2} of the Fe²⁺ [37], the peak at 725.0 eV was associated towards the binding energies of 2p_{1/2} of Fe²⁺ and Fe³⁺ [38] and the peak at 718.3 eV served as a satellite for the afore mentioned four peaks, demonstrating the coexistence of Fe²⁺ and Fe³⁺ in the catalyst [14,34]. For the XPS of the Cu 2p sections, the peak located at 932.8 eV is attributed to the Cu(I) molecule. The Cu 2p_{3/2} peak at 934.0 eV and its shakeup satellite are linked with Cu(II) [17]. The peak occurring at 952.7 eV with a satellite at 961.6 eV was attributed to Cu 2p_{1/2} (Fig. 3g) [39-41].

Optical studies: The optical characteristics of the synthesized nanoparticles *viz.* ZrO₂, g-C₃N₄, CuFe₂O₄ and nanocomposite ZrO₂/g-C₃N₄/CuFe₂O₄ were analyzed using the diffuse reflectance spectroscopy (DRS) as shown in Fig. 4. The absorption threshold value of ZrO₂/g-C₃N₄/CuFe₂O₄ nanocomposite has extended up to the wider range of UV-visible light and the primary adsorption edge of pure g-C₃N₄ appeared at 440 nm [42], ZrO₂ appeared at 250 nm [37], CuFe₂O₄ appeared at 390 nm [43] and ZrO₂/g-C₃N₄/CuFe₂O₄ nanocomposite appeared at 460 nm (Fig. 4a). Therefore, the band edge of ZrO₂/g-C₃N₄/CuFe₂O₄ nanocomposite is greater than that of pure nanocomponents. The bandgap energies of the direct transition semiconductor might be calculated by a plot of (αhv)² vs. the photo energy (hv) according to Kubelka-Munk function [44]. As a result, the bandgaps of ZrO₂, g-C₃N₄, CuFe₂O₄ and ZrO₂/g-C₃N₄/CuFe₂O₄ nanocomposite were 4.26, 2.72, 1.92 and 2.3 eV, respectively (Fig. 4b). The diffuse reflectance spectra are converted into the Kubelka-Munk function using the following relation:

$$F(R) = \frac{(1 \times R)^2}{2R} \quad (2)$$

where R stands for measured reflectance.

The bandgap energy (E_g) value is estimated using Tauc equation:

$$(\alpha hv)^2 = A(hv - E_g) \quad (3)$$

where hv is the photon energy and A is the constant, α-absorption coefficient. Plotting of (αhv)² or [F(R)hv]² vs. (hv) enables to calculate the bandgap energy with the help of extrapolating of linear fit. This technique is frequently applied to semiconductors [4,9].

Photoluminescence study: Fig. 5 shows the fluorescence (PL) spectra of pure ZrO₂, g-C₃N₄, CuFe₂O₄ and ZrO₂/g-C₃N₄/CuFe₂O₄ nanocomposite samples with excitation wavelength range of 400-480 nm. It could be observed that pure g-C₃N₄ has a strong fluorescence emission peak at about 441 nm due to its high recombination rate of photoinduced holes and electrons [34,36]. In terms of ZrO₂, CuFe₂O₄ and ZrO₂/g-C₃N₄/CuFe₂O₄ nanocomposite photocatalysts, the PL intensities significantly decreased due to the heterostructures, reducing the recombination of photoexcited electron/hole pairs. Moreover, 445 nm was the quenching of intrinsic fluorescence of ZrO₂ and the PL intensities of CuFe₂O₄ and ternary ZrO₂/g-C₃N₄/CuFe₂O₄ nanocomposites were 432 nm and 407 nm, respectively [45]. The

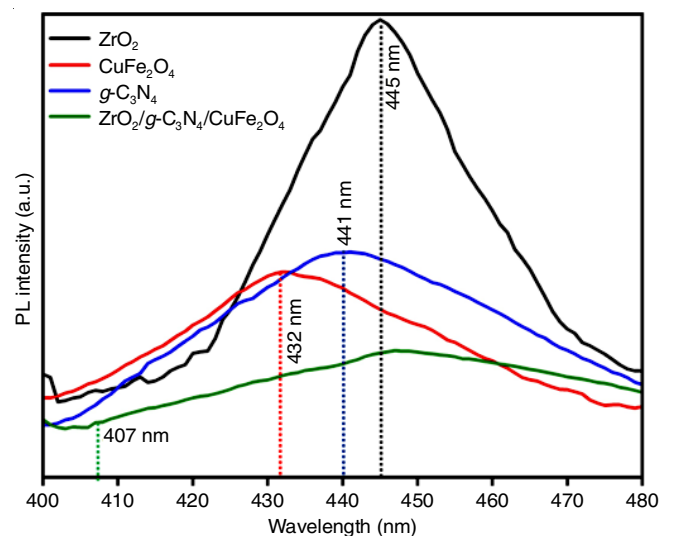


Fig. 5. Photoluminescence (PL) spectra of ZrO₂, CuFe₂O₄, g-C₃N₄ and ZrO₂/g-C₃N₄/CuFe₂O₄ materials

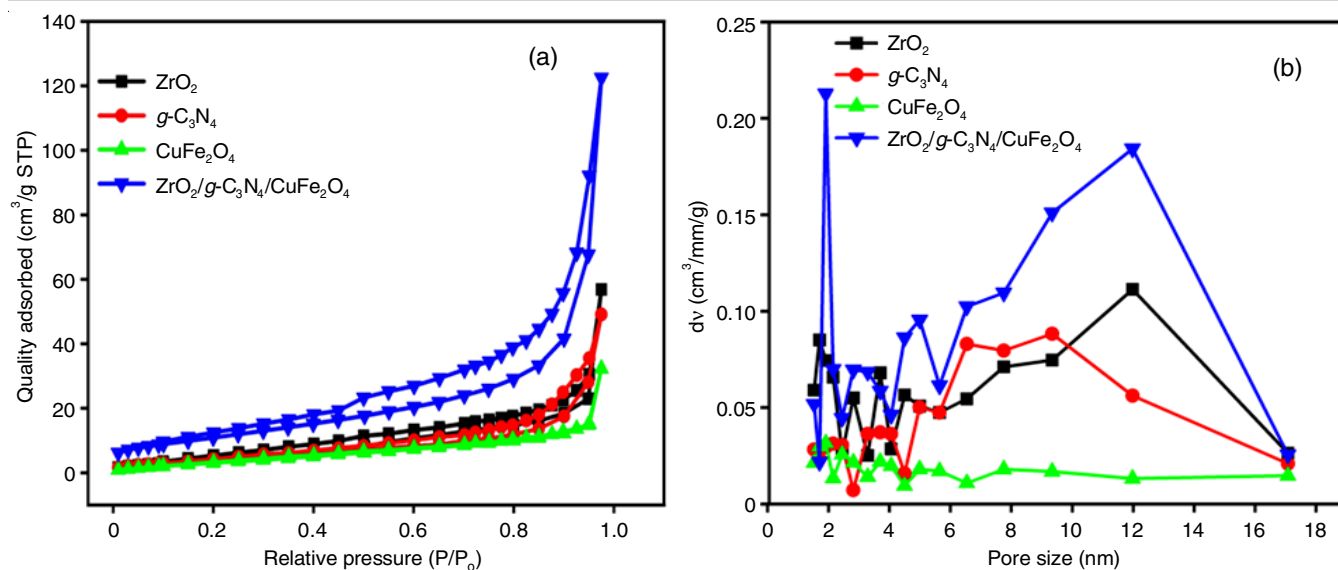


Fig. 6. (a) N₂ adsorption-desorption isotherms of ZrO₂, g-C₃N₄, CuFe₂O₄ as well as ZrO₂/g-C₃N₄/CuFe₂O₄ nanocomposite, (b) BJH pore-size distribution

intensity of peak ZrO₂/g-C₃N₄/CuFe₂O₄ composite is weaker than ZrO₂, g-C₃N₄ and CuFe₂O₄, which indicated that the photo-induced electrons and holes were recombining at a slower rate [34]. It was determined that the ZrO₂/g-C₃N₄/CuFe₂O₄ nanocomposite have exhibited better photocatalytic activity.

Surface analysis: The surface features of the synthesized catalysts were analyzed using the Brunauer-Emmet-Teller (BET) and Barrett-Joyner-Halenda (BJH) methods. Fig. 6a shows the N₂ adsorption and desorption isotherm of the synthesized nanocomponents and nanocomposite. The N₂ adsorption-desorption isotherms of the samples have shown a hysteresis loop, indicating the presence of mesoporous solids, with pore size between 2 and 17 nm (Fig. 6b). The specific surface area of CuFe₂O₄, g-C₃N₄, ZrO₂, and ZrO₂/g-C₃N₄/CuFe₂O₄ nanocomposite are 14.75 m²/g, 18.25 m²/g, 26.50 m²/g and 41.40 m²/g. The pore diameter values CuFe₂O₄, g-C₃N₄, ZrO₂ and ZrO₂/g-C₃N₄/CuFe₂O₄ nanocomposite were 0.0500 nm, 0.0760 nm, 0.0074 nm and 0.140 nm, respectively [46,47]. The S_{BET} of ZrO₂/g-C₃N₄/CuFe₂O₄ nanocomposite is larger than that of ZrO₂, g-C₃N₄, CuFe₂O₄ nanoparticles. From Table-1, it was found that the specific area, pore volume and pore size of ZrO₂/g-C₃N₄/CuFe₂O₄ nanocomposite was greater than of ZrO₂, g-C₃N₄ and CuFe₂O₄ nanoparticles [48]. The mesoporous nature and large surface area of ZrO₂/g-C₃N₄/CuFe₂O₄ nanocomposite support the presence of highly effective active sites. It might be beneficial to aqueous penetration in the photocatalytic reaction [49].

TABLE-1

SURFACE AREA, PORE VOLUME AND PORE SIZES OF ZrO₂, g-C₃N₄, CuFe₂O₄ AND ZrO₂/g-C₃N₄/CuFe₂O₄ NANOCOMPOSITE

Sample	Surface area (m ² /g)	Pore volume (cc/g)	Pore size (nm)
CuFe ₂ O ₄	14.75	13.5	0.0500
g-C ₃ N ₄	18.25	16.4	0.0760
ZrO ₂	26.50	24.4	0.0074
ZrO ₂ /g-C ₃ N ₄ /CuFe ₂ O ₄	41.40	38.0	0.1400

Charge transfer and conductivity studies: Fig. 7 displays the EIS Nyquist plots of g-C₃N₄, ZrO₂, CuFe₂O₄ and ZrO₂/g-C₃N₄/CuFe₂O₄ nanocomposite electrode with irradiation of visible light. The radius of arc in the spectra indicates the separation of charge and resistance of transfer at the electrode, the radius was smaller and the charge separation was higher efficiency [50]. The ZrO₂/g-C₃N₄/CuFe₂O₄ nanocomposite electrode shows smaller radius of arc than pure ZrO₂, g-C₃N₄ and CuFe₂O₄ in visible light irradiation, revealed that the composite has a better charge transfer and conductivity than pure ZrO₂, g-C₃N₄ and CuFe₂O₄. The results of photoelectrochemical characterization indicate that the ZrO₂/g-C₃N₄/CuFe₂O₄ nanocomposite could effectively enhance the photogenerated charge separation efficiency than the ZrO₂, g-C₃N₄ and CuFe₂O₄. These results indicated the separation and transfer efficiency of photogenerated electron-hole pairs increased, which further confirmed

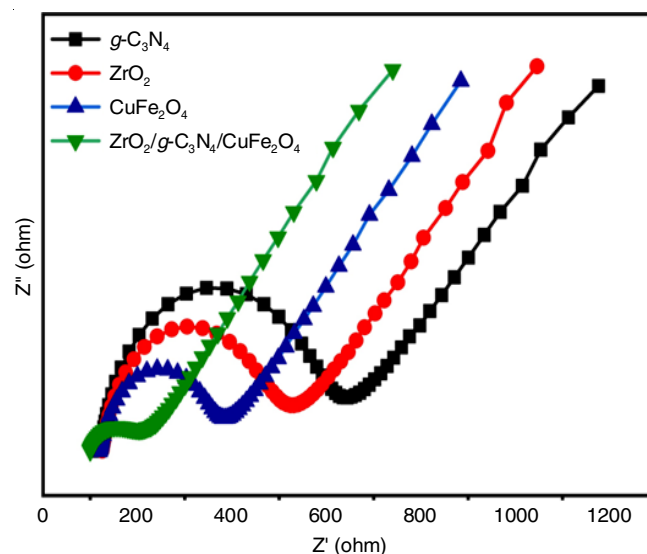


Fig. 7. Electron impedance spectroscopy of g-C₃N₄, ZrO₂, CuFe₂O₄ and ZrO₂/g-C₃N₄/CuFe₂O₄ under visible light irradiation, λ 1~ 420 nm

that $\text{ZrO}_2/g\text{-C}_3\text{N}_4/\text{CuFe}_2\text{O}_4$ nanocomposite possessed enhanced photocatalytic activity [51,52].

Photocatalytic activity: The photocatalytic activity of the $\text{ZrO}_2/g\text{-C}_3\text{N}_4/\text{CuFe}_2\text{O}_4$ nanocomposite was analyzed towards the degradation of the different kinds of pollutants such as amoxicillin (antibiotics), methylene blue (dye) and chlorpyrifos (pesticide) under dark and visible light conditions.

Photocatalytic degradation of amoxicillin: The efficiency of photocatalysis of $g\text{-C}_3\text{N}_4$, ZrO_2 , CuFe_2O_4 nanocatalysts and $\text{ZrO}_2/g\text{-C}_3\text{N}_4/\text{CuFe}_2\text{O}_4$ nanocomposite were evaluated by the photodegradation of aqueous amoxicillin solution under visible light irradiation. The decreasing in the intensity of amoxicillin (λ_{max} 341 nm) by UV absorption peak confirmed the amoxicillin photodegradation related to the irradiation time t (min) [24]. Fig. 8a-d shows the degradation of pollutant by $g\text{-C}_3\text{N}_4$, ZrO_2 , CuFe_2O_4 and $\text{ZrO}_2/g\text{-C}_3\text{N}_4/\text{CuFe}_2\text{O}_4$ nanocomposite. Among them, 64.60% pollutant was degraded by the $\text{ZrO}_2/g\text{-C}_3\text{N}_4/\text{CuFe}_2\text{O}_4$ nanocomposite under UV-visible light radiation for about 90 min. The rate constant (Fig. 9a) and the degradation efficiency of $g\text{-C}_3\text{N}_4$, ZrO_2 , CuFe_2O_4 and $\text{ZrO}_2/g\text{-C}_3\text{N}_4/\text{CuFe}_2\text{O}_4$ nanocomposites were calculated (Fig. 9b) and

the pseudo-first-order kinetics of photodegradation of amoxicillin were also calculated (Fig. 9c). The results clearly showed that $\text{ZrO}_2/g\text{-C}_3\text{N}_4/\text{CuFe}_2\text{O}_4$ nanocomposite has the higher rate constant (0.0109 min^{-1}) for amoxicillin than that of individual nanocomponents (Fig. 14). The superior photocatalytic activity of $\text{ZrO}_2/g\text{-C}_3\text{N}_4/\text{CuFe}_2\text{O}_4$ nanocomposite could be attributing to the highly feasible photo-excited e^-/h^+ pair transfer/separation on the surface of nanocatalysts [12]. Moreover, in optimum addition of ZrO_2 and CuFe_2O_4 in $g\text{-C}_3\text{N}_4$ was showed the higher enhancing degradation, signifying that the higher amount of UV-visible light absorption ability and larger hindrance of photo-excited recombination centre also promoted the oxidant species for amoxicillin degradation [14,53].

Photocatalytic degradation of chlorpyrifos: The photocatalyst efficiencies of $g\text{-C}_3\text{N}_4$, ZrO_2 , CuFe_2O_4 and $\text{ZrO}_2/g\text{-C}_3\text{N}_4/\text{CuFe}_2\text{O}_4$ nanocomposite for chlorpyrifos solution under UV-visible light irradiation were evaluated. The decreasing in the intensity of chlorpyrifos (λ_{max} 291 nm) by UV absorbance peaks confirmed the chlorpyrifos photodegradation related to the radiation time t (min) [24]. Fig. 10a-d shows the degradation of pollutant by $g\text{-C}_3\text{N}_4$, ZrO_2 , CuFe_2O_4 and $\text{ZrO}_2/g\text{-C}_3\text{N}_4/\text{CuFe}_2\text{O}_4$

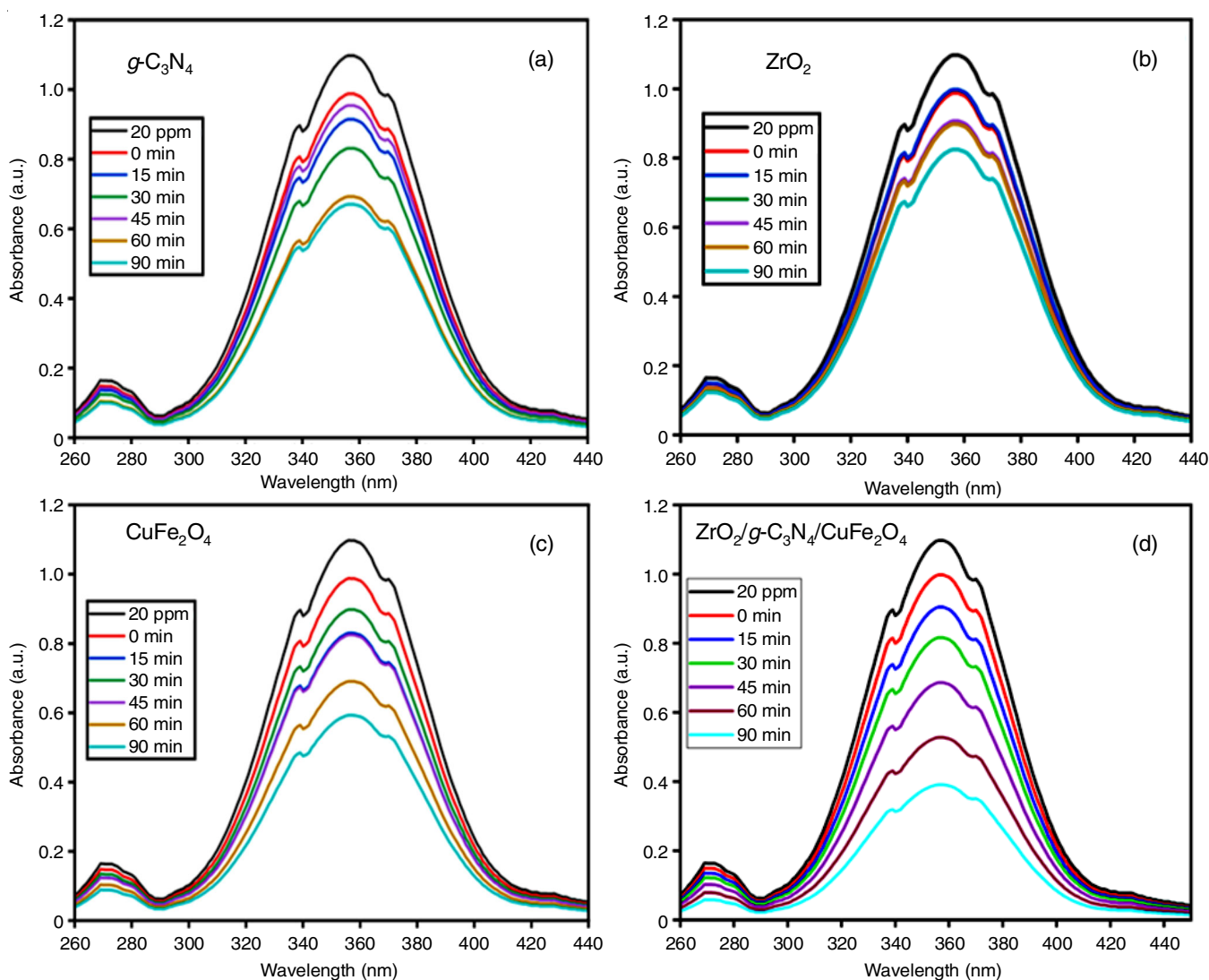


Fig. 8. Photocatalytic degradation of amoxicillin (AMX) with (a) $g\text{-C}_3\text{N}_4$, (b) ZrO_2 , (c) CuFe_2O_4 and (d) $\text{ZrO}_2/g\text{-C}_3\text{N}_4/\text{CuFe}_2\text{O}_4$

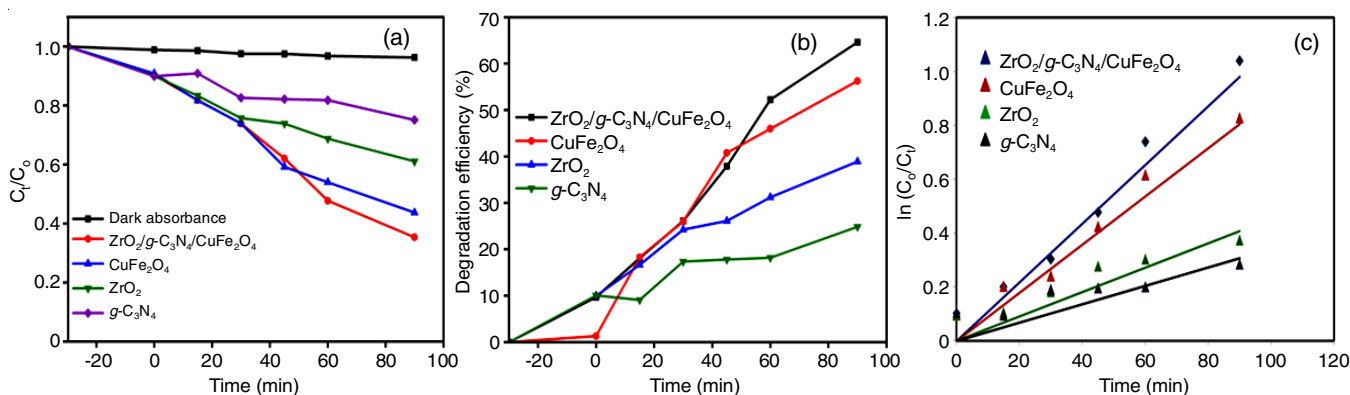


Fig. 9. Amoxicillin (AMX) (a) photodegradation rate, (b) photodegradation efficiency and (c) pseudo-first-order kinetic plots for CPF over the obtained photocatalytic samples of photocatalyst $g\text{-C}_3\text{N}_4$, ZrO_2 , CuFe_2O_4 and $\text{ZrO}_2/g\text{-C}_3\text{N}_4/\text{CuFe}_2\text{O}_4$

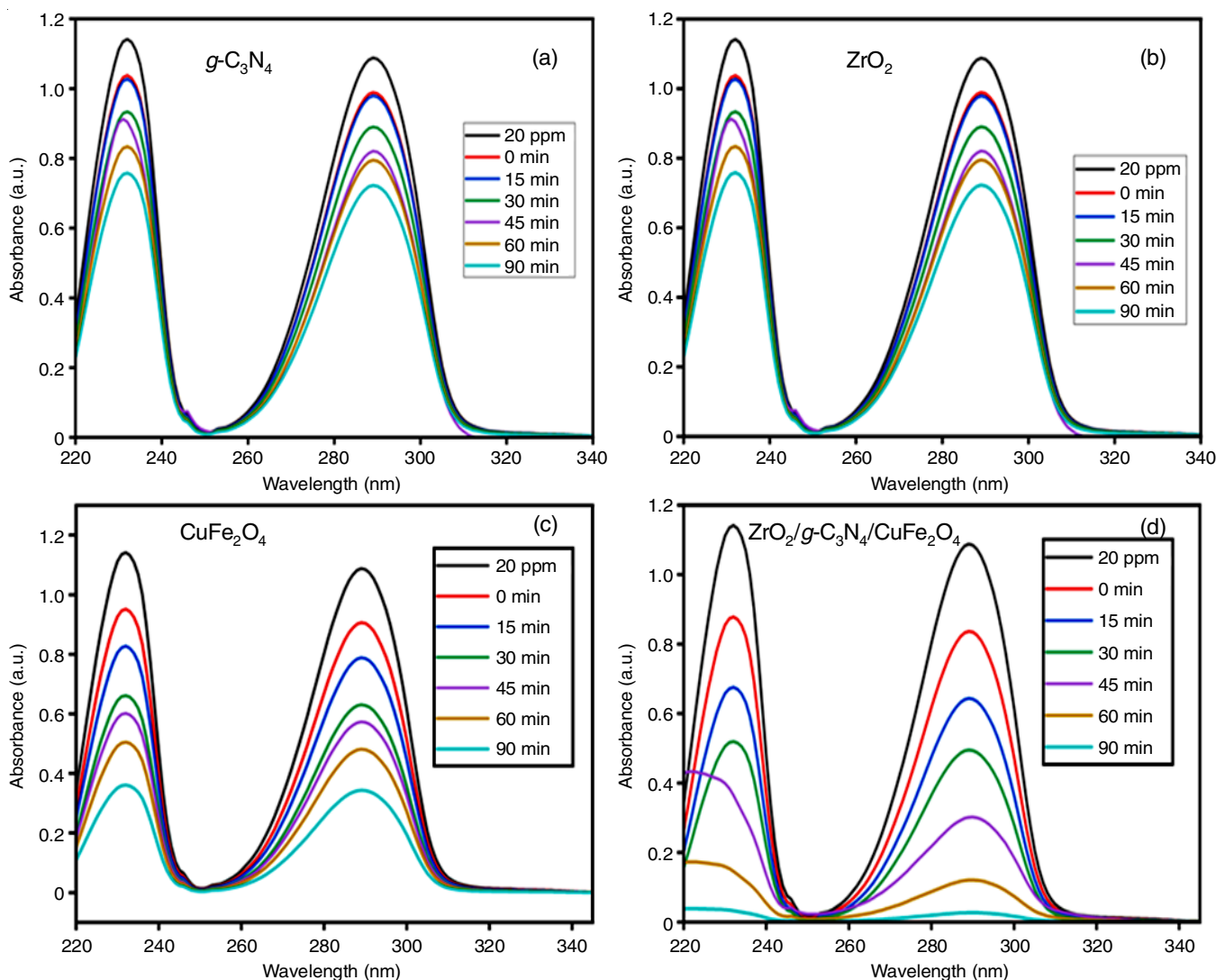


Fig. 10. Photocatalytic degradation of chlorpyrifos (CPF) with (a) $g\text{-C}_3\text{N}_4$, (b) ZrO_2 , (c) CuFe_2O_4 and (d) $\text{ZrO}_2/g\text{-C}_3\text{N}_4/\text{CuFe}_2\text{O}_4$

nanocomposite. Among them, 97.30% pollutant was degraded by the $\text{ZrO}_2/g\text{-C}_3\text{N}_4/\text{CuFe}_2\text{O}_4$ nanocomposite under UV-visible light irradiation for about 90 min. The degradation rate constant (Fig. 11a), the degradation efficiency (Fig. 11b) and the pseudo-first-order kinetics of photodegradation of chlorpyrifos were calculated (Fig. 11c). The results clearly indicated that the $\text{ZrO}_2/$

$g\text{-C}_3\text{N}_4/\text{CuFe}_2\text{O}_4$ nanocomposite has the higher rate constant (0.0367 min^{-1}) for chlorpyrifos than that of individual nanocomponents (Fig. 14). The superior photocatalytic activity of $\text{ZrO}_2/g\text{-C}_3\text{N}_4/\text{CuFe}_2\text{O}_4$ nanocomposite might be attributing to the greater feasible photo-excited e^-/h^+ pair transfer/separation on the surface of nanocatalysts [10]. Furthermore, the addition

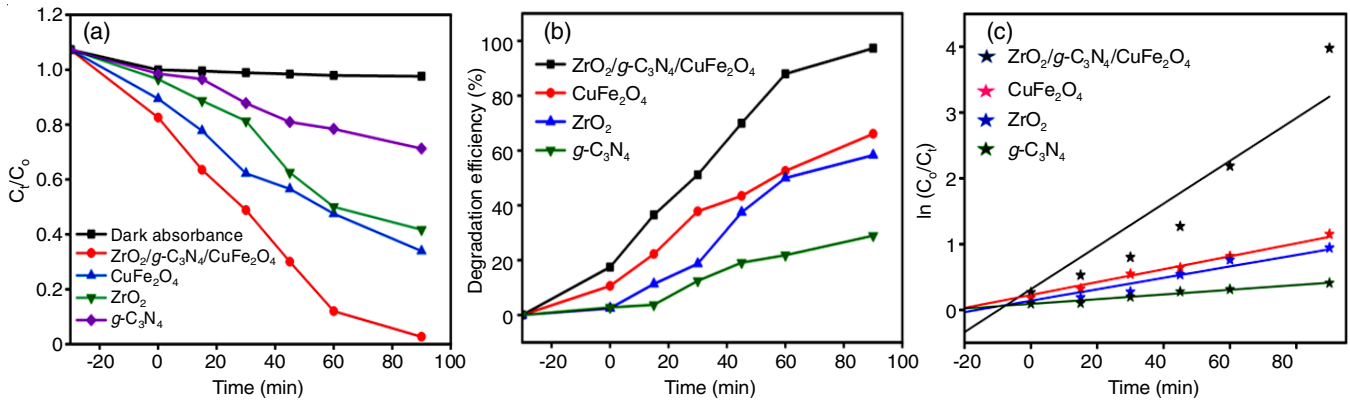


Fig. 11. Chlorpyrifos (CPF) (a) photodegradation rate, (b) photodegradation efficiency and (c) pseudo-first-order kinetic plots for CPF over the obtained photocatalytic samples of $g\text{-C}_3\text{N}_4$, ZrO_2 , CuFe_2O_4 and $\text{ZrO}_2/g\text{-C}_3\text{N}_4/\text{CuFe}_2\text{O}_4$

of ZrO_2 and CuFe_2O_4 in $g\text{-C}_3\text{N}_4$ showed the higher degradation efficiency, which is attributed to the higher hindrance of photo-excited recombination centre and also promoted the oxidant species for the chlorpyrifos degradation [14,54].

Photocatalytic degradation of methylene blue: The photocatalyst efficiencies of $g\text{-C}_3\text{N}_4$, ZrO_2 , CuFe_2O_4 nanocatalysts

and $\text{ZrO}_2/g\text{-C}_3\text{N}_4/\text{CuFe}_2\text{O}_4$ nanocomposite were evaluated by the photodegradation of methylene blue solution under UV-visible light irradiation. The decreasing in the intensity of MB dye (λ_{max} 664 nm) by UV absorbance peaks confirmed the photodegradation of methylene blue with respect to the radiation time t (min) [24]. Fig. 12a-d shows the degradation of pollutant

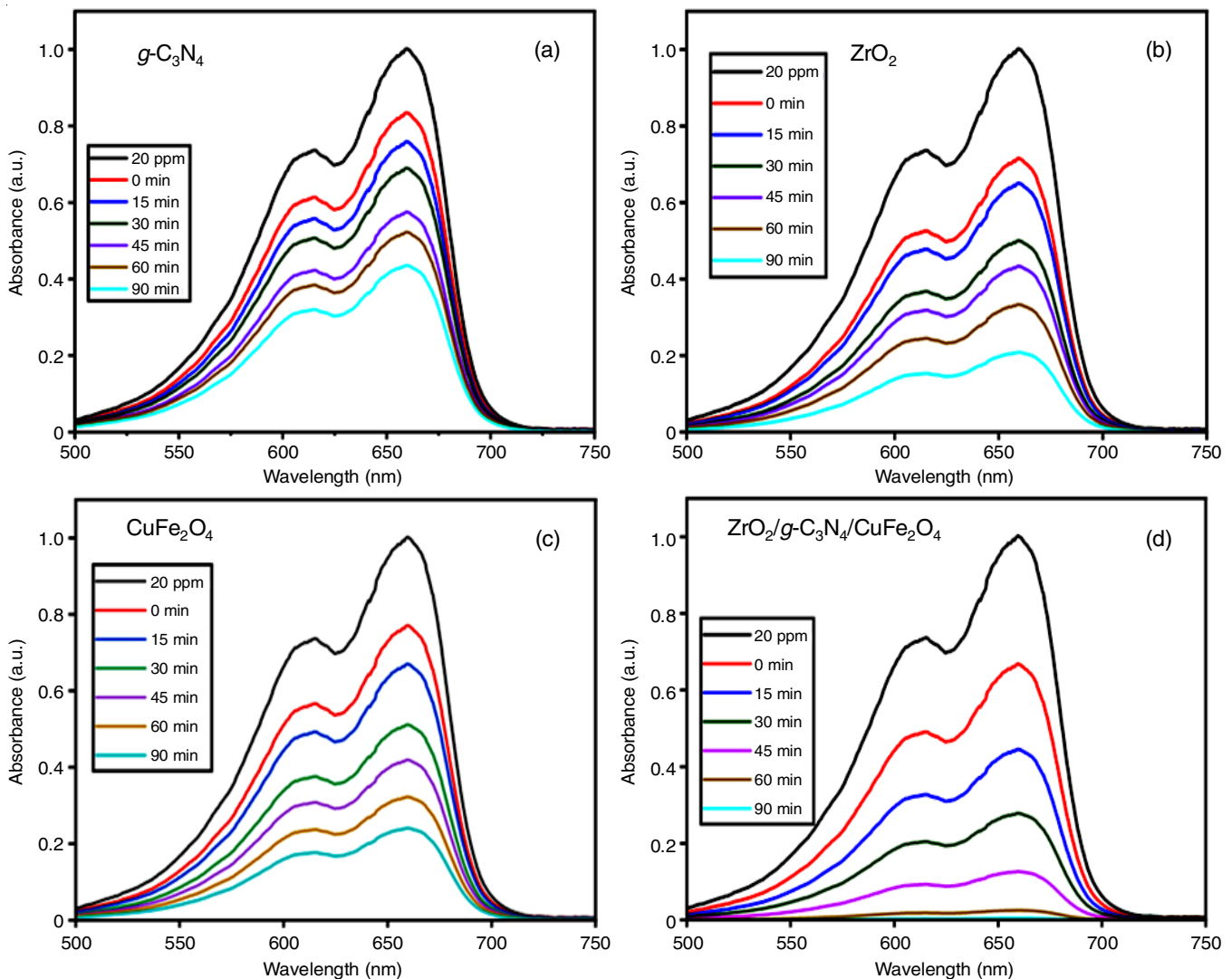


Fig. 12. Methylene blue (MB) photocatalytic degradation of (a) $g\text{-C}_3\text{N}_4$, (b) ZrO_2 , (c) CuFe_2O_4 and (d) $\text{ZrO}_2/g\text{-C}_3\text{N}_4/\text{CuFe}_2\text{O}_4$

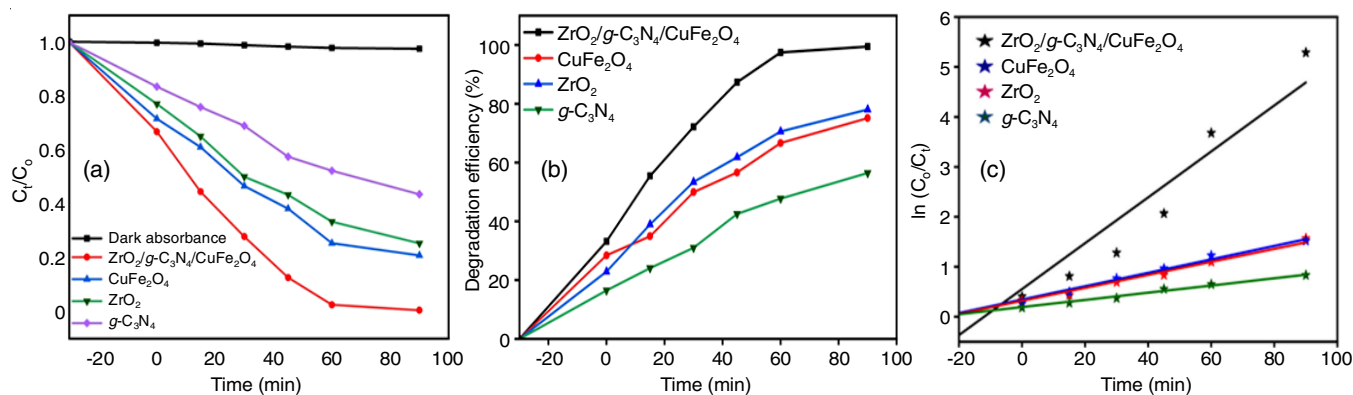


Fig. 13. Methylene blue (MB) (a) photodegradation rate constant, (b) photodegradation efficiency and (c) pseudo-first-order kinetic plots for MB over the photocatalytic samples of $g\text{-C}_3\text{N}_4$, ZrO_2 , CuFe_2O_4 and $\text{ZrO}_2/g\text{-C}_3\text{N}_4/\text{CuFe}_2\text{O}_4$

by $g\text{-C}_3\text{N}_4$, ZrO_2 , CuFe_2O_4 and $\text{ZrO}_2/g\text{-C}_3\text{N}_4/\text{CuFe}_2\text{O}_4$ nanocomposite. Among them, 99.40% pollutant was degraded by the $\text{ZrO}_2/g\text{-C}_3\text{N}_4/\text{CuFe}_2\text{O}_4$ nanocomposite under UV-visible light radiation for about 90 min. The degradation rate constant (Fig. 13a), the degradation efficiency (Fig. 13b) and the pseudo-first-order kinetics of photodegradation of methylene blue were calculated (Fig. 13c). The results clearly indicated that the $\text{ZrO}_2/g\text{-C}_3\text{N}_4/\text{CuFe}_2\text{O}_4$ nanocomposite has the larger rate constant (0.0533 min^{-1}) for MB dye than that of individual nanocomponents (Fig. 14). The superior photocatalytic activity of $\text{ZrO}_2/g\text{-C}_3\text{N}_4/\text{CuFe}_2\text{O}_4$ nanocomposite might be attributing to the highly feasible photo-excited e^-/h^+ pair transfer/separation on the surface of nanocatalysts.

Effect of scavengers: Various scavengers has been utilized in the photocatalytic process for reactive species of scavenge [29,30]. In this present work, three active oxidizing species (O_2^- , h^+ and OH^\bullet) could be produced and participate in this reaction. The benzoquinone (BQ) was employed to capture O_2^- , while ethylenediaminetetraacetic acid (EDTA) and isopropanol (IPA) are used to capture h^+ and OH^\bullet during AMX/CPF/MB photocatalytic degradation with the $\text{ZrO}_2/g\text{-C}_3\text{N}_4/\text{CuFe}_2\text{O}_4$ nanocomposite photocatalyst under visible light, respectively. The efficiency of AMX degradation decreased from 97.60% (no scavengers) to 47.80% (EDTA), 52.90% (IPA) and 81.20% (BQ), respectively [49] (Fig. 15). Likewise, the efficiency of CPF degradation decreased from 97.30% (no scavengers) to 42.80% (EDTA), 59.30% (IPA) and 80.10% (BQ) [10] and for

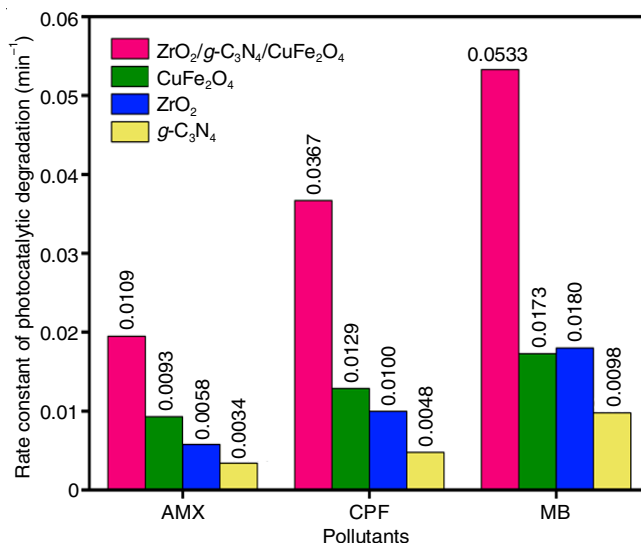


Fig. 14. Highest to lowest rate constant of photocatalytic degradation activities of amoxicillin (AMX), chlorpyrifos (CPF) and methylene blue (MB) by $\text{ZrO}_2/g\text{-C}_3\text{N}_4/\text{CuFe}_2\text{O}_4$ nanocomposite, CuFe_2O_4 , ZrO_2 and $g\text{-C}_3\text{N}_4$

MB molecules, the degradation decreased from 99.40% (no scavengers) to 31.20% (EDTA), 82.30% (IPA) and 40.30% (BQ) [55], respectively (Fig. 15). These results showed the participation of reactive species in the pollutants degradation is of the order of $\text{BQ} > \text{IPA} > \text{EDTA}$ revealing that h^+ was more effective than OH^\bullet and O_2^- for AMX/CPF and $\text{IPA} > \text{BQ} >$

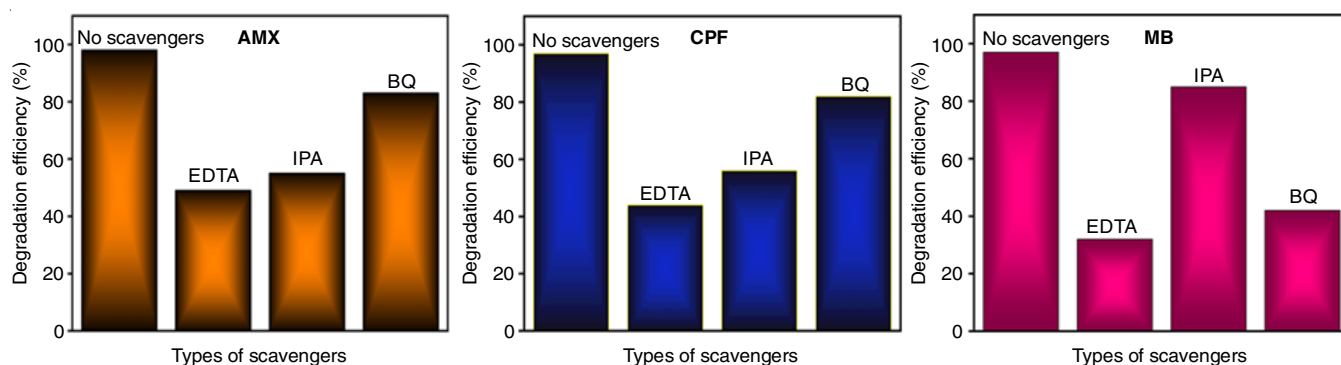


Fig. 15. Effect of reactive scavenging species on the amoxicillin (AMX), chlorpyrifos (CPF) and methylene blue (MB) pollutants photodegradation activity over the $\text{ZrO}_2/g\text{-C}_3\text{N}_4/\text{CuFe}_2\text{O}_4$ photocatalytic nanocomposite under visible-light exposure

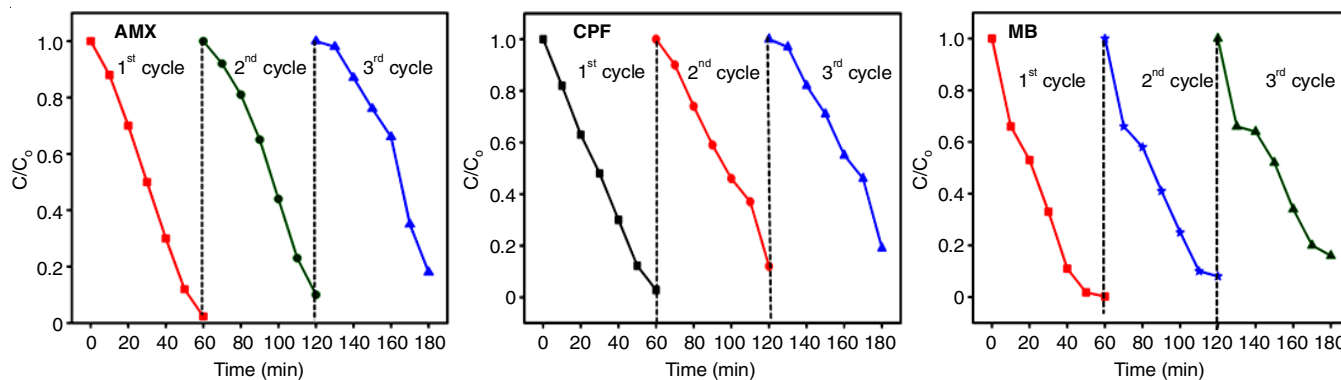


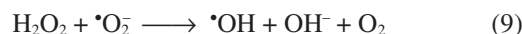
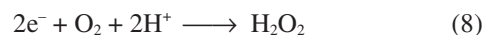
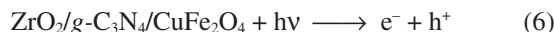
Fig. 16. Recycling stability performance over the $\text{ZrO}_2/g\text{-C}_3\text{N}_4/\text{CuFe}_2\text{O}_4$ photocatalytic nanocomposite

EDTA revealing h^+ was more effective than $\cdot\text{O}_2^-$ and $\cdot\text{OH}$ for MB molecules. Similar results are reported by Balarak *et al.* [56] for identified the reactive species.

Reusability studies: Photocatalyst stability was evaluated by the recyclability of $\text{ZrO}_2/g\text{-C}_3\text{N}_4/\text{CuFe}_2\text{O}_4$ nanocomposite of three cycling experiments were carried out for amoxicillin/methylene blue/chlorpyrifos molecules photodegradation. After every cycle, samples were centrifuged, completely rinsed with deionized water to eliminate any remaining contaminants and also dried in an oven at 60°C for the following cycles. At 90 min interval between each cycle, $\sim 64.60\%$ of amoxicillin was decomposed in first cycle, which was slightly lower ($\sim 4\%$) than that of second cycle ($\sim 60.30\%$) and third cycle ($\sim 55.90\%$) (Fig. 16). For chlorpyrifos, 97.30% was decomposed in the first cycle, which was slightly, lower ($\sim 5\%$) than that of second cycle ($\sim 92.20\%$) and third cycle ($\sim 87.30\%$). For methylene blue, 99.40% was decomposed in the first cycle, which was slightly, lower ($\sim 3\%$) than that of second cycle ($\sim 96.70\%$) and third cycle ($\sim 92.80\%$) [57]. From The XRD patterns of $\text{ZrO}_2/g\text{-C}_3\text{N}_4/\text{CuFe}_2\text{O}_4$ nanocomposite before and after three photo-reactions are shown in Fig. 17. The major diffraction peak positions are unaltered, after the third photoreaction, indicating that $\text{ZrO}_2/g\text{-C}_3\text{N}_4/\text{CuFe}_2\text{O}_4$ nanocomposite is a stable photocatalyst. The above results indicated that $\text{ZrO}_2/g\text{-C}_3\text{N}_4/\text{CuFe}_2\text{O}_4$ nanocomposite showed high-stability under visible light irradi-

ation due to the $\pi\text{-}\pi$ stacking interaction between the ZrO_2 , $g\text{-C}_3\text{N}_4$ and CuFe_2O_4 nanocatalysts [10,14].

Photocatalytic mechanism: The proposed mechanism explains the photocatalytic degradation of organic pollutants (AMX/CPF/MB) over the $\text{ZrO}_2/g\text{-C}_3\text{N}_4/\text{CuFe}_2\text{O}_4$ nanocomposite (**Scheme-I**). During the photocatalysis under irradiation of visible light, electrons and holes generated, the electrons were excited from valence band (VB) to conduction band (CB) and holes were created on the VB [14,58]. As $g\text{-C}_3\text{N}_4$, narrow bandgap material having extremely negative charged e^- from CB of $g\text{-C}_3\text{N}_4$ easily transferred to CB of $\text{ZrO}_2/\text{CuFe}_2\text{O}_4$ and the highly positive charged h^+ from VB of $\text{ZrO}_2/\text{CuFe}_2\text{O}_4$ is transferred to VB of $g\text{-C}_3\text{N}_4$, creating a heterojunction that separates the charge carries, substantially decreases the possibilities of recombination [34]. As a result, enhanced the photocatalytic activity of the nanomaterial. Thereafter the generated e^- and h^+ react with O_2 and OH^- produce $\cdot\text{O}_2^-$ and $\cdot\text{OH}$ radicals [59]. This radical has a tendency to decompose the organic dye into H_2O and CO_2 compounds. Therefore, presence of $\text{ZrO}_2/g\text{-C}_3\text{N}_4/\text{CuFe}_2\text{O}_4$ nanocomposite promoted the high photocatalytic activity of the nanocomposite corresponds to the high separation of charges as well as easy transfer of photoinduced charge carriers [49].



Thus, both enhanced surface area and improve UV-visible light irradiation absorption ability in case of the $\text{ZrO}_2/g\text{-C}_3\text{N}_4/\text{CuFe}_2\text{O}_4$ nanocomposite lead to the rapid degradation efficiency towards the studied organic pollutants [3].

Conclusion

A novel $\text{ZrO}_2/g\text{-C}_3\text{N}_4/\text{CuFe}_2\text{O}_4$ photocatalytic nanocomposite was successfully synthesized by wet impregnation method and characterized using XRD, FTIR, TEM, EDS, XPS, UV-DRS, PL, BET and EIS techniques. The homogeneous distribution of the components in the nanocomposite was confirmed

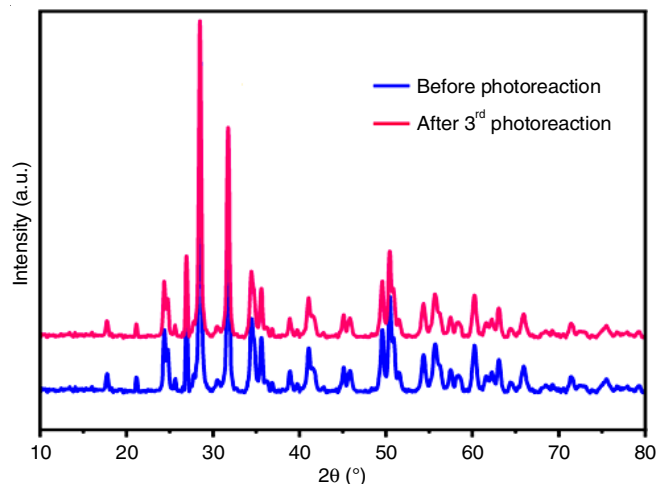
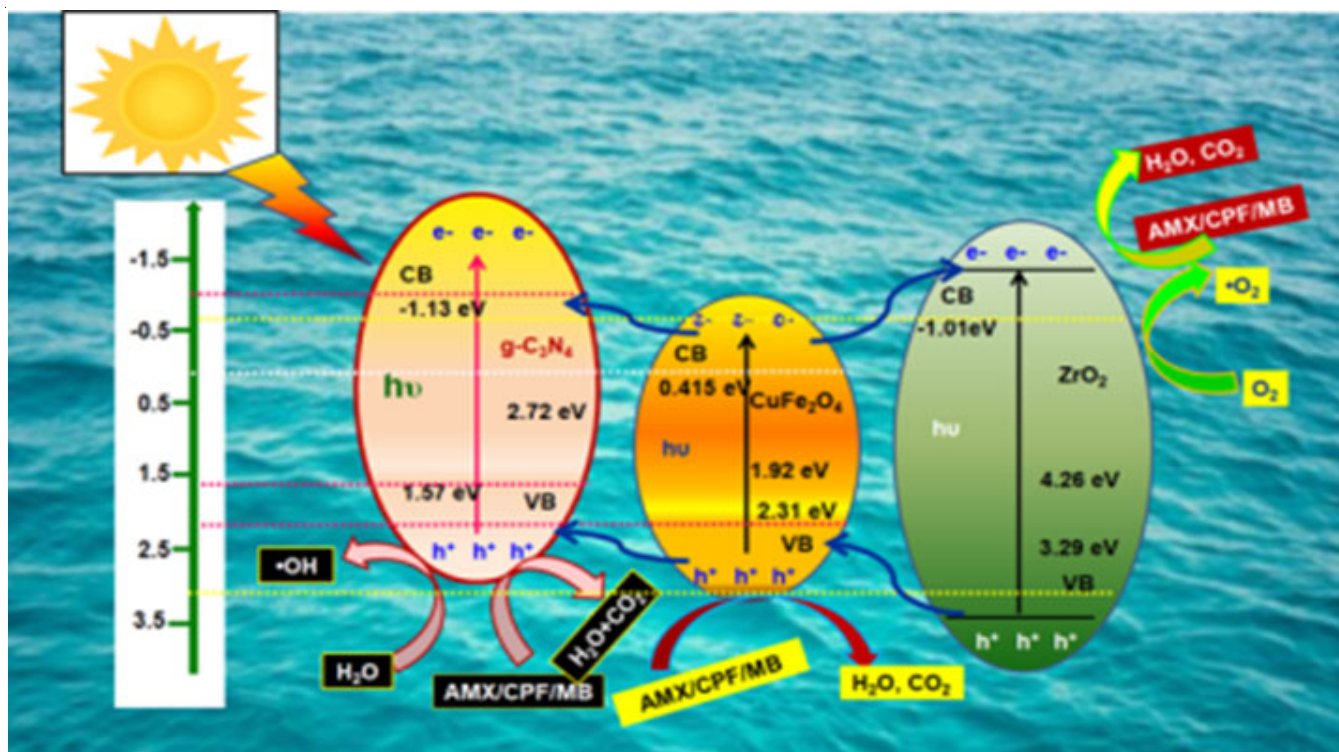


Fig. 17. XRD patterns of $\text{ZrO}_2/g\text{-C}_3\text{N}_4/\text{CuFe}_2\text{O}_4$ before and after third photo-reactions



Scheme-I: The possible reaction mechanism of AMX/CPF/MB in $\text{ZrO}_2/\text{g-C}_3\text{N}_4/\text{CuFe}_2\text{O}_4$ nanocomposite system

by EDS spectra. The rate constant values of degradation for the novel synthesized $\text{ZrO}_2/\text{g-C}_3\text{N}_4/\text{CuFe}_2\text{O}_4$ nanocomposite were 0.0109, 0.0367 and 0.0533 min^{-1} for amoxicillin (64.60%), chlorpyrifos (97.30%) and methylene blue (99.40%), respectively. These values were 2.5 times higher than those of CuFe_2O_4 , 3 times higher than those of ZrO_2 and 5.5 times higher than those of $\text{g-C}_3\text{N}_4$. After three successive recycling experiments, the novel nanocomposite was effortlessly retrieved and exhibited reasonably good durability and stability. Hence, this study focused on the synthesis of novel $\text{ZrO}_2/\text{g-C}_3\text{N}_4/\text{CuFe}_2\text{O}_4$ nanocomposite as a highly efficient photocatalyst for the degradation of organic contaminants in aqueous environments.

ACKNOWLEDGEMENTS

This work was financially supported by the Tamil Nadu Open University Research Fellowship (TNOURF), Tamil Nadu Open University, Chennai, India.

CONFLICT OF INTEREST

The authors declare that there is no conflict of interests regarding the publication of this article.

REFERENCES

- M. Verma and A.K. Haritash, *Environ. Technol. Innov.*, **20**, 101072 (2020); <https://doi.org/10.1016/j.eti.2020.101072>
- D. Huang, X. Sun, Y. Liu, H. Ji, W. Liu, C.-C. Wang, W. Ma and Z. Cai, *Chin. Chem. Lett.*, **32**, 2787 (2021); <https://doi.org/10.1016/j.ccllet.2021.01.012>
- A. Mirzaei, Z. Chen, F. Haghighat and L. Yerushalmi, *Appl. Catal. B.* (2018); <https://doi.org/10.1016/j.apcatb.2018.10.009>
- T.S. Anirudhan, F. Shainy, V.C. Sekhar and V.S. Athira, *J. Photochem. Photobiol. Chem.*, **418**, 113333 (2021); <https://doi.org/10.1016/j.jphotochem.2021.113333>
- Z. Liu, W. Zhang, Q. Liang, J. Huang, B. Shao, Y. Liu, Q. He, T. Wu, J. Gong, M. Yan and W. Tang, *Environ. Sci. Pollut. Res. Int.*, **28**, 42683 (2021); <https://doi.org/10.1007/s11356-021-13694-z>
- A.E. Hassan, M.H. Elsayed, M.S.A. Hussien, M.G. Mohamed, S.-W. Kuo, H.-H. Chou, I.S. Yahia, T.A. Mohamed and Z. Wen, *Int. J. Hydrogen Energy*, **48**, 9620 (2023); <https://doi.org/10.1016/j.ijhydene.2022.12.009>
- I. Ali and J.-O. Kim, *Mater. Chem. Phys.*, **261**, 124246 (2021); <https://doi.org/10.1016/j.matchemphys.2021.124246>
- S. Khan, J.S. Park and T. Ishihara, *Catalysts*, **13**, 196 (2023); <https://doi.org/10.3390/catal13010196>
- Yu. Lin, X. Liu, Z. Liu and Y. Xu, *Small*, **17**, 2103348 (2021); <https://doi.org/10.1002/smll.202103348>
- A.M. Ismael, A.N. El-Shazly, S.E. Gaber, M.M. Rashad, A.H. Kamel and S.S.M. Hassan, *RSC Adv.*, **10**, 34806 (2020); <https://doi.org/10.1039/D0RA02874F>
- S. Munir, A. Rasheed, S. Zulfiqar, M. Aadil, P.O. Agboola, I. Shakir and M.F. Warsi, *Ceram. Int.*, **46**, 29182 (2020); <https://doi.org/10.1016/j.ceramint.2020.08.091>
- M. Sayadi, H. Ahmadpour and S. Homaeigozar, *Nanomaterials*, **11**, 298 (2021); <https://doi.org/10.3390/nano11020298>
- T. Dou, L. Zang, Y. Zhang, Z. Sun, L. Sun and C. Wang, *Mater. Lett.*, **244**, 151 (2019); <https://doi.org/10.1016/j.matlet.2019.02.066>
- R. Rajendran, S. Vignesh, V. Raj, B. Palanivel, A.M. Ali, M.A. Sayed and M. Shkir, *J. Alloys Compd.*, **894**, 162498 (2021); <https://doi.org/10.1016/j.jallcom.2021.162498>
- B.M.B. Ensano, L. Borea, V. Naddeo, V. Belgiorno, M.D.G. de Luna, M. Balakrishnan and F.C. Ballesteros Jr., *J. Hazard. Mater.*, **361**, 367 (2019); <https://doi.org/10.1016/j.jhazmat.2018.07.093>
- E.A. Serna-Galvis, J. Silva-Agredo, A.M. Botero-Coy, A. Moncayo-Lasso, F. Hernández and R.A. Torres-Palma, *Sci. Total Environ.*, **670**, 623 (2019); <https://doi.org/10.1016/j.scitotenv.2019.03.153>

17. H. Nadais, X. Li, N. Alves, C. Couras, H.R. Andersen, I. Angelidaki and Y. Zhang, *Chem. Eng. J.*, **338**, 401 (2018); <https://doi.org/10.1016/j.cej.2018.01.014>
18. F. Martínez, R. Molina, I. Rodríguez, M.I. Pariente, Y. Segura and J.A. Melero, *J. Environ. Chem. Eng.*, **6**, 485 (2018); <https://doi.org/10.1016/j.jece.2017.12.008>
19. Y. Ouarda, B. Tiwari, A. Azaïs, M.-A. Vaudreuil, S.D. Ndiaye, P. Drogui, R.D. Tyagi, S. Sauvé, M. Desrosiers, G. Buelna and R. Dubé, *Chemosphere*, **193**, 160 (2018); <https://doi.org/10.1016/j.chemosphere.2017.11.010>
20. A.G. Trovó, R.F. Pupo Nogueira, A. Agüera, A.R. Fernandez-Alba and S. Malato, *Water Res.*, **45**, 1394 (2011); <https://doi.org/10.1016/j.watres.2010.10.029>
21. J.Y. Shen, Z.S. Cui, Z.W. Wu, J.X. Wang, Q. Ning and X.M. Lü, *Mater. Res. Innov.*, **19**, 187 (2014); <https://doi.org/10.1179/1433075X14Y.0000000240>
22. G. Palanisamy, K. Bhuvaneshwari, A. Chinnadurai, G. Bharathi and T. Pazhanivel, *J. Phys. Chem. Solids*, (2019); <https://doi.org/10.1016/j.jpcs.2019.109231>
23. P. Deng, M. Gan, X. Zhang, Z. Li and Y. Hou, *Int. J. Hydrogen Energy*, **44**, 30084 (2019); <https://doi.org/10.1016/j.ijhydene.2019.09.129>
24. D. Zhu and Q. Zhou, *Appl. Catal. B*, **281**, 119474 (2021); <https://doi.org/10.1016/j.apcatb.2020.119474>
25. S. Zinatloo-Ajabshir and M. Salavati-Niasari, *J. Mol. Liq.*, **216**, 545 (2016); <https://doi.org/10.1016/j.molliq.2016.01.062>
26. K. Prasad, D.V. Pinjari, A.B. Pandit and S.T. Mhaske, *Ultrason. Sonochem.*, **18**, 1128 (2011); <https://doi.org/10.1016/j.ultsonch.2011.03.001>
27. S.A. Soomro, I.H. Gul, H. Naseer, S. Marwat and M. Mujahid, *Curr. Nanosci.*, **15**, 420 (2018); <https://doi.org/10.2174/1573413714666181115122016>
28. Z. Zhu, X. Li, Q. Zhao, Y. Li, C. Sun and Y. Cao, *Mater. Res. Bull.*, **48**, 2927 (2013); <https://doi.org/10.1016/j.materresbull.2013.04.042>
29. D.P. Ojha, H.P. Karki and H.J. Kim, *J. Ind. Eng. Chem.*, **61**, 87 (2018); <https://doi.org/10.1016/j.jiec.2017.12.004>
30. V.B. Shevale, A.G. Dhodamani and S.D. Delekar, *ACS Omega*, **5**, 1098 (2020); <https://doi.org/10.1021/acsomega.9b03260>
31. M. Khan, H. Farah, N. Iqbal, T. Noor, M.Z.B. Amjad and S.S. Ejaz Bukhari, *RSC Adv.*, **11**, 37575 (2021); <https://doi.org/10.1039/D1RA07796A>
32. M.B. Tahir, M. Sagir and K. Shahzad, *J. Hazard. Mater.*, **363**, 205 (2019); <https://doi.org/10.1016/j.jhazmat.2018.09.055>
33. E.V. Siddhardhan, S. Surender and T. Arumanayagam, *Inorg. Chem. Commun.*, **147**, 110244 (2023); <https://doi.org/10.1016/j.inoche.2022.110244>
34. R. Li, M. Cai, Z. Xie, Q. Zhang, Y. Zeng, H. Liu, G. Liu and W. Lv, *Appl. Catal. B*, **244**, 974 (2018); <https://doi.org/10.1016/j.apcatb.2018.12.043>
35. X. Cao, X. Yang, T. Wu, B. Tang and P. Guo, *J. Mater. Civ. Eng.*, **31**, 04019031 (2019); [https://doi.org/10.1061/\(ASCE\)MT.1943-5533.0002580](https://doi.org/10.1061/(ASCE)MT.1943-5533.0002580)
36. Y. Yao, F. Lu, Y. Zhu, F. Wei, X. Liu, C. Lian and S. Wang, *J. Hazard. Mater.*, **297**, 224 (2015); <https://doi.org/10.1016/j.jhazmat.2015.04.046>
37. M. Zarei, *Water-Energy Nexus*, **3**, 135 (2020); <https://doi.org/10.1016/j.wen.2020.08.002>
38. L. Kong, J. Wang, X. Mu, R. Li, X. Li, X. Fan, P. Song, F. Ma and M. Sun, *Mater. Today Energy*, **13**, 11 (2019); <https://doi.org/10.1016/j.mtener.2019.04.011>
39. H. Liu, J. Liang, S. Fu, L. Li, J. Cui, P. Gao, F. Zhao and J. Zhou, *Colloids Surf. A Physicochem. Eng. Asp.*, **591**, 124552 (2020); <https://doi.org/10.1016/j.colsurfa.2020.124552>
40. D. Gao, Y. Liu, P. Liu, M. Si and D. Xue, *Sci. Rep.*, **6**, 35768 (2016); <https://doi.org/10.1038/srep35768>
41. D. Rathore, S. Mitra, R. Kurchania and R.K. Pandey, *J. Mater. Sci. Mater. Electron.*, **29**, 1925 (2017); <https://doi.org/10.1007/s10854-017-8102-0>
42. K. Kombaiyah, J.J. Vijaya, L.J. Kennedy, M. Bououdina and B. Al-Najar, *J. Phys. Chem. Solids*, **115**, 162 (2017); <https://doi.org/10.1016/j.jpcs.2017.12.024>
43. J. Jin, H. Yan, Q. Bie, G. Wang and G. Su, *IOP Conf. Ser. Earth Environ. Sci.*, **825**, 012034 (2021); <https://doi.org/10.1088/1755-1315/825/1/012034>
44. J. Huang, D. Li, R. Li, P. Chen, Q. Zhang, H. Liu, W. Lv, G. Liu and Y. Feng, *J. Hazard. Mater.*, **386**, 121634 (2019); <https://doi.org/10.1016/j.jhazmat.2019.121634>
45. L. Zheng, X. Xiao, Y. Li and W. Zhang, *Trans. Nonferrous Met. Soc. China*, **27**, 1117 (2017); [https://doi.org/10.1016/S1003-6326\(17\)60130-4](https://doi.org/10.1016/S1003-6326(17)60130-4)
46. X. Guo, Y. Xu, K. Wang, F. Zha, X. Tang and H. Tian, *Res. Chem. Intermed.*, **46**, 853 (2019); <https://doi.org/10.1007/s11164-019-03994-y>
47. O. Alduhaish, M. Ubaidullah, A.M. Al-Enizi, N. Alhokbany, S.M. Alshehri and J. Ahmed, *Sci. Rep.*, **9**, 14139 (2019); <https://doi.org/10.1038/s41598-019-50780-2>
48. S. Keerthana, R. Yuvakkumar, G. Ravi, S. Pavithra, M. Thambidurai, C. Dang and D. Velauthapillai, *Environ. Res.*, **200**, 111528 (2021); <https://doi.org/10.1016/j.envres.2021.111528>
49. D. Balarak, N. Mengelizadeh, P. Rajiv and K. Chandrika, *Environ. Sci. Pollut. Res. Int.*, **28**, 49743 (2021); <https://doi.org/10.1007/s11356-021-13525-1>
50. M.N. Arifin, K.M.R. Karim, H. Abdullah and M.R. Khan, *Bull. Chem. React. Eng. Catal.*, **14**, 219 (2019); <https://doi.org/10.9767/bcrec.14.1.3616.219-227>
51. R. Zhao, X. Sun, Y. Jin, J. Han, L. Wang and F. Liu, *J. Mater. Sci.*, **54**, 5445 (2019); <https://doi.org/10.1007/s10853-018-03278-7>
52. J. Zhao, X. Chen, Y. Zhou, H. Tian, Q. Guo and X. Hu, *Res. Chem. Intermed.*, **46**, 1805 (2020); <https://doi.org/10.1007/s11164-019-04064-z>
53. I.F. Silva, I.F. Teixeira, R.D.F. Rios, G.M. do Nascimento, I. Binatti, H.F.V. Victória, K. Krambrock, L.A. Cury, A.P.C. Teixeira and H.O. Stumpf, *J. Hazard. Mater.*, **401**, 123713 (2021); <https://doi.org/10.1016/j.jhazmat.2020.123713>
54. J. Farner Budarz, E.M. Cooper, C. Gardner, E. Hodzic, P.L. Ferguson, C.K. Gunsch and M.R. Wiesner, *J. Hazard. Mater.*, **372**, 61 (2019); <https://doi.org/10.1016/j.jhazmat.2017.12.028>
55. R. Rajendran, K. Varadharajan, V. Jayaraman, B. Singaram and J. Jeyaram, *Appl. Nanosci.*, **8**, 61 (2018); <https://doi.org/10.1007/s13204-018-0652-9>
56. D. Balarak, T.J. Al-Musawi, I.A. Mohammed and H. Abasizadeh, *SN Appl. Sci.*, **2**, 1015 (2020); <https://doi.org/10.1007/s42452-020-2841-x>
57. K. Vignesh, A. Suganthi, B.-K. Min and M. Kang, *J. Mol. Catal. Chem.*, **395**, 373 (2014); <https://doi.org/10.1016/j.molcata.2014.08.040>
58. D. Zhang, S. Cui and J. Yang, *J. Alloys Compd.*, **708**, 1141 (2017); <https://doi.org/10.1016/j.jallcom.2017.03.095>
59. S. Narzary, K. Alamelu, V. Raja and B.M. Jaffar Ali, *J. Environ. Chem. Eng.*, **8**, 104373 (2020); <https://doi.org/10.1016/j.jece.2020.104373>